

# Molecular bases for the selection of the chromophore of animal rhodopsins

Hoi Ling Luk<sup>a</sup>, Federico Melaccio<sup>b</sup>, Silvia Rinaldi<sup>b</sup>, Samer Gozem<sup>a</sup>, and Massimo Olivucci<sup>a,b,1</sup>

<sup>a</sup>Department of Chemistry, Bowling Green State University, Bowling Green, OH 43403; and <sup>b</sup>Dipartimento di Biotecnologie, Chimica e Farmacia, Università di Siena, Siena I-53100, Italy

Edited by Arieh Warshel, University of Southern California, Los Angeles, CA, and approved October 28, 2015 (received for review May 26, 2015)

The functions of microbial and animal rhodopsins are triggered by the isomerization of their all-*trans* and 11-*cis* retinal chromophores, respectively. To lay the molecular basis driving the evolutionary transition from the all-*trans* to the 11-*cis* chromophore, multiconfigurational quantum chemistry is used to compare the isomerization mechanisms of the sensory rhodopsin from the cyanobacterium *Anabaena* PCC 7120 (ASR) and of the bovine rhodopsin (Rh). It is found that, despite their evolutionary distance, these eubacterial and vertebrate rhodopsins start to isomerize via distinct implementations of the same bicycle-pedal mechanism originally proposed by Warshel [Warshel A (1976) *Nature* 260:678–683]. However, by following the electronic structure changes of ASR (featuring the all-*trans* chromophore) during the isomerization, we find that ASR enters a region of degeneracy between the first and second excited states not found in Rh (featuring the 11-*cis* chromophore). We show that such degeneracy is modulated by the preorganized structure of the chromophore and by the position of the reactive double bond. It is argued that the optimization of the electronic properties of the chromophore, which affects the photoisomerization efficiency and the thermal isomerization barrier, provided a key factor for the emergence of the striking amino acid sequence divergence observed between the microbial and animal rhodopsins.

rhodopsin | retinal chromophore | ultrafast isomerization | excited states | computational photobiology

Rhodopsins (also called retinal or retinylidene proteins) are a family of membrane proteins found in all life domains (1). All members of the family bind a retinal chromophore and display either light-sensing, light-powered ion-pumping or light-gated ion-channeling activities. These functions are carried out by a common protein architecture featuring seven  $\alpha$ -helices (I–VII in Fig. 1A) forming a cavity with a chromophore-binding lysine located in the middle of helix VII.

Despite their striking structural similarity, microbial (type I) and animal (type II) rhodopsins display a negligible amino acid sequence identity that is also reflected in dramatically different chromophore cavities. Although this would indicate that type I and type II rhodopsins have evolved in parallel from different ancestors, Theobald and coworkers (2, 3) have recently provided experimental evidence in favor of a single common ancestor. If this is the case, one is left with the problem of understanding the mechanisms that could have led to the drastic divergence in the amino acid sequences. Here, we investigate the role played by the transition to a different chromophore in such a process.

Type I and type II rhodopsins feature different retinal chromophores. Whereas type I rhodopsins have an all-*trans* chromophore (PSBAT in Fig. 1A and B), type II rhodopsins incorporate an 11-*cis* chromophore (PSB11 in Fig. 1A and B). PSBAT and PSB11 are responsible for the activation of the protein function that is triggered by the photoisomerization of their C13=C14 and C11=C12 double bond, respectively. However, the fact that PSB11 is thermodynamically unstable with respect to PSBAT indicates that PSB11 might have been selected to carry out an otherwise inaccessible function. In fact, given the basic role of the chromophore in the rhodopsin machinery, it is conceivable that the optimization

of distinctive PSB11 functions would have led to an extreme divergence. To investigate whether such functions exist, we compare the isomerization mechanisms (see curly arrows in Fig. 1B and C) of PSBAT, PSB13, and PSB11 at an atomic resolution. To do so we use computer models of microbial and vertebrate light-sensing rhodopsins (4, 5). The simulations unveil electronic effects not achievable by PSBAT and barely achievable in PSB13, directly related to the higher photoisomerization speed reported for type II rhodopsins and, in turn, to the control of the isomerization quantum efficiency (6–10).

The properties of the retinal chromophore are modulated by its interaction with the protein environment (11–16). For this reason, we simulate the chromophore isomerization in complete models of the sensory rhodopsin from the cyanobacterium *Anabaena* PCC 7120 (ASR) and of the visual pigment of the bovine retina (Rh), type I and a type II rhodopsins, respectively. ASR exists in two thermostable forms, ASR<sub>AT</sub> and ASR<sub>13C</sub>, featuring the 15-*anti*-PSBAT and 15-*syn*-PSB13 chromophores (Fig. 1B), respectively. Upon light irradiation, the chromophores isomerize about the C13=C14 double bond to generate the corresponding K intermediate (see Fig. 1C for ASR<sub>13C</sub>). Because ASR<sub>AT</sub>-K and ASR<sub>13C</sub>-K convert thermally to ASR<sub>13C</sub> and ASR<sub>AT</sub>, respectively, ASR displays a photochromic cycle (17). Such a photochromism is not observed in Rh, where irradiation causes the photoisomerization of PSB11 to PSBAT with formation of bathoRh. This is then thermally converted to states that interact with a transducer and hydrolyze the chromophore–lysine linkage (18).

The photoisomerization of Rh has been extensively investigated. Spectroscopic studies have shown that it occurs on a subpicosecond timescale with an S<sub>1</sub> decay occurring in less than 100 fs (7, 19, 20). Furthermore, the observation of ground-state (S<sub>0</sub>) vibrational coherence (21) points to a direct transfer of the

## Significance

Microbial and animal rhodopsins share several striking structural features including a seven  $\alpha$ -helix fold and a highly conserved active-site lysine in the seventh helix. However, these protein families lack significant similarity in their amino acid sequence. In this paper we address the question of why the sequence of animal rhodopsins, featuring an 11-*cis* chromophore, could have diverged from a microbial ancestor incorporating the more stable all-*trans* chromophore. We show that, by using light-responsive computer models of a eubacterial sensory rhodopsin and of a vertebrate visual rhodopsin, it is possible to identify a distinctive electronic character of the 11-*cis* chromophore that could have become an effective target for natural selection.

Author contributions: M.O. designed research; H.L.L. performed research; H.L.L., F.M., S.R., S.G., and M.O. analyzed data; and H.L.L., F.M., S.R., S.G., and M.O. wrote the paper.

The authors declare no conflict of interest.

This article is a PNAS Direct Submission.

<sup>1</sup>To whom correspondence should be addressed. Email: molivuc@bgsu.edu.

This article contains supporting information online at [www.pnas.org/lookup/suppl/doi:10.1073/pnas.1510262112/-DCSupplemental](http://www.pnas.org/lookup/suppl/doi:10.1073/pnas.1510262112/-DCSupplemental).

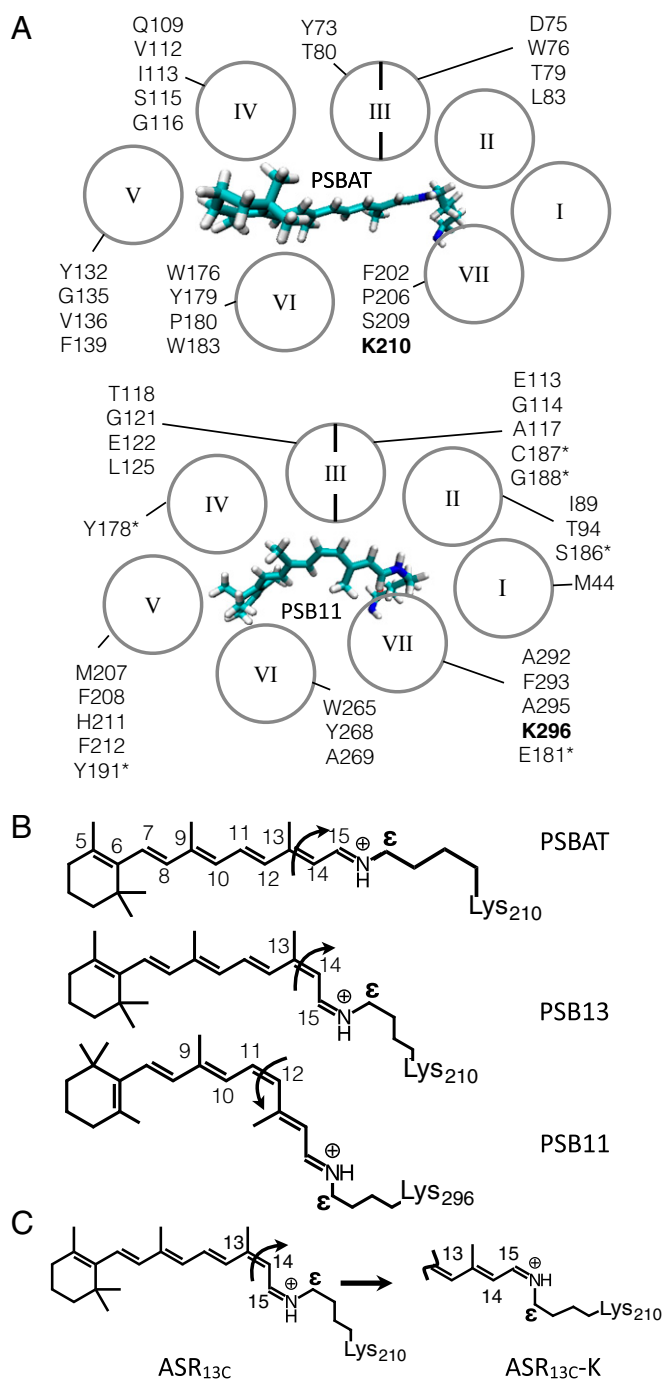


**Fig. 1.** Rhodopsin structure. (A) Chromophore cavities of a type I (Upper, *Anabaena* PCC 7120) and a type II (Lower, *Bos taurus*) sensory rhodopsin. The cavity amino acids are given in one-letter code according to their  $\alpha$ -helix location. Asterisk indicates the loop connecting helices IV and V. The chromophore-binding lysins are in bold. (B) Structures of the chromophores of ASR<sub>AT</sub> (Upper), ASR<sub>13C</sub> (Middle), and Rh (Lower). The curly arrows indicate the reactive double bond. (C) ASR<sub>13C</sub> → ASR<sub>13C</sub>-K chromophore isomerization reaction.

first excited state ( $S_1$ ) population to the photoproduct passing through a  $S_1/S_0$  conical intersection (CI) without involving higher excited states (e.g.,  $S_2$ ). Such a mechanism has been computationally documented (22–24) and experimentally tracked by infrared probing (24). ASR<sub>AT</sub> and ASR<sub>13C</sub> have been spectroscopically investigated by Ruhman and coworkers (25) and Haacke and coworkers (26, 27). The results indicate that in ASR<sub>13C</sub> the

chromophore accesses the CI more quickly (0.10–0.15 ps) than in ASR<sub>AT</sub> (0.50–0.75 ps), showing a dynamics closer to that of Rh (0.08 ps). Such timescales have been found to be consistent with potential energy surface mapping and trajectory computations (23, 24, 28, 29).

The results revised above provide the basis for investigating the photoisomerization of type I and type II rhodopsins. Accordingly, we use multiconfigurational quantum chemistry (MCQC)-based quantum-mechanics/molecular-mechanics (QM/MM) models (30) of ASR<sub>AT</sub>, ASR<sub>13C</sub> and Rh to simulate their electronic and geometrical changes up to 200 fs after the electronic excitation. We show that the magnitude of the observed timescales correlate with the mixing of the  $S_1$  and  $S_2$  states and that such mixing does not occur in the PSB11 containing Rh. It is argued that this fact connects the optimization of the chromophore electronic properties to a higher light sensitivity of animal rhodopsins.

## Results and Discussion

**Absorption Maxima.** As documented in the *SI Appendix* [see *SI Appendix, section 1* for the testing of alternative protocols ranked for their ability to yield ASR models of comparable quality to the Rh model (31)], the  $S_0$  models of ASR<sub>AT</sub> and ASR<sub>13C</sub> reproduce the vertical excitation energies ( $\Delta E_{S_1-S_0}$ ) associated with the observed absorption maximum ( $\lambda_{\max}^a$ ) value within a few kilocalories per mole (+1.5 and +1.0 kcal·mol<sup>-1</sup> for ASR<sub>AT</sub> and ASR<sub>13C</sub>, respectively; see *SI Appendix, section 2.1* for all computed and observed excitation energy values). The origin of the  $\lambda_{\max}^a$  values is investigated by isolating the chromophores from their protein environment and recomputing their  $\Delta E_{S_1-S_0}$  without geometrical relaxation (this quantity is, usually, red-shifted compared with that of the protein due to the lack of effects stabilizing  $S_0$ ). We also looked at the vertical  $S_1-S_2$  energy gap ( $\Delta E_{S_2-S_1}$ ) that will be discussed in the next sections. It is found that, for all models, the electrostatic effect of the protein is responsible for 7–8 kcal·mol<sup>-1</sup> increase and 3–4 kcal·mol<sup>-1</sup> decrease in  $\Delta E_{S_1-S_0}$  and  $\Delta E_{S_2-S_1}$ , respectively. Since the protein has a systematic effect, the changes are due to the chromophore geometries that display excitation energy differences replicating those computed for the corresponding proteins. For instance, the isolated Rh chromophore has  $\Delta E_{S_1-S_0}$  and  $\Delta E_{S_2-S_1}$  values  $\sim 5$  and  $\sim 3$  kcal·mol<sup>-1</sup> larger than the corresponding ASR<sub>AT</sub> chromophore values. These data parallel the  $\sim 4$  and  $\sim 3$  kcal·mol<sup>-1</sup> differences obtained for the chromophore in Rh and ASR<sub>13C</sub>. These  $\Delta E_{S_1-S_0}$  and  $\Delta E_{S_2-S_1}$  changes are assigned to the out-of-plane twisting of the  $\beta$ -ionone ring (the C5–C6–C7–C8 dihedral angle is  $-56^\circ$ ) in Rh (32, 33), which decreases the conjugation with respect to the more planar ASR chromophores (see top structures in Fig. 2 A–C). Note that both the  $\Delta E_{S_1-S_0}$  and  $\Delta E_{S_2-S_1}$  values decrease when increasing the chromophore conjugation (*SI Appendix, section 2.2*).

**Trajectory Calculations.** The photoisomerization dynamics of ASR<sub>AT</sub> and ASR<sub>13C</sub> are investigated by running single  $S_1$  trajectories starting from the corresponding  $S_0$  equilibrium structures with zero initial velocities (Franck–Condon trajectories) (34). The computations are carried on until the trajectories enter the region of a  $S_1/S_0$  CI or reach 200 fs. We assume that during such an ultrashort time the trajectory describes the average evolution of the corresponding  $S_1$  population. This has been assessed for both Rh (23, 24, 31) and ASR models (*SI Appendix, section 3*). As shown in Fig. 2 A and B, ASR<sub>AT</sub> remains on  $S_1$  for the entire duration of the trajectory whereas ASR<sub>13C</sub> reaches the CI after *ca.* 150 fs. The estimated  $S_1$  lifetimes are consistent with the available transient spectroscopy measurements and computations (25, 29) showing that the ASR<sub>AT</sub> photoisomerizes at least five times more slowly than ASR<sub>13C</sub>. However, ASR<sub>13C</sub> seems to react in a timescale only slightly slower than that computed for Rh (31) (Fig. 2C), consistent with the observations (25, 26).

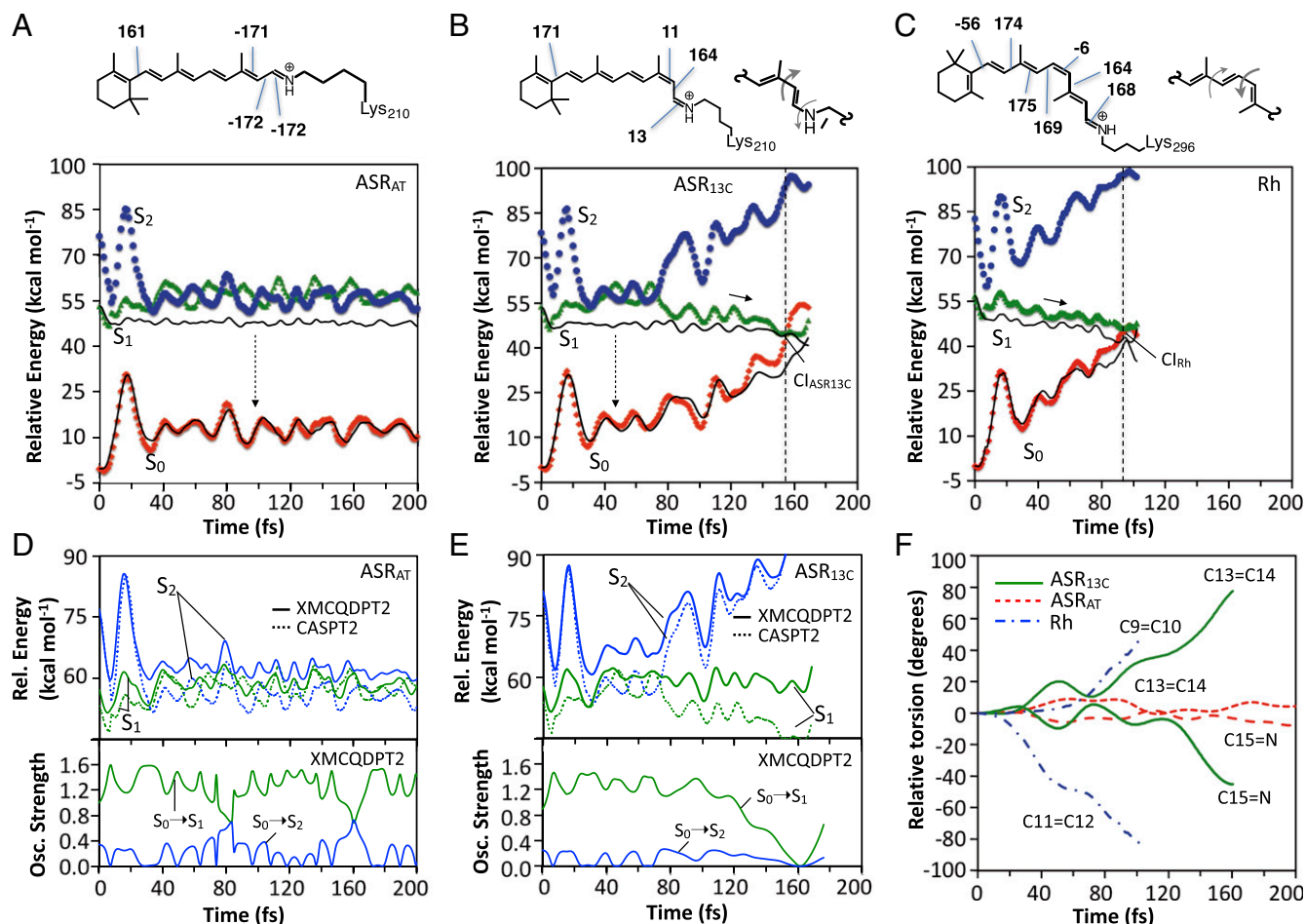


**Fig. 2.** QM/MM trajectories of ASR<sub>AT</sub>, ASR<sub>13C</sub>, and Rh computed at the two root state average scaled-CASSCF/Amber (black lines) level of theory and corrected at the CASPT2 (23) and XMCQDPT2 levels (35). (A) S<sub>0</sub> (filled diamonds), S<sub>1</sub> (filled triangles), and S<sub>2</sub> (filled circles) CASPT2/CASSCF/Amber energy profiles along the ASR<sub>AT</sub> trajectory. The main out-of-plane (deviation larger than ±5°) dihedral angles of the chromophore S<sub>0</sub> equilibrium structure are given at the top. The vertical dashed arrow represents weak fluorescence. (B) Same data for ASR<sub>13C</sub> with representation (at Top) of the bicycle pedal motion driving the isomerization on S<sub>1</sub> in which the bond order is reversed. The vertical dashed arrow represents weak fluorescence. (C) Same data for the Rh trajectory. (D) View of the XMCQDPT2 (solid line) and CASPT2 (dotted line) S<sub>1</sub> and S<sub>2</sub> energy profiles (Upper) and oscillator strengths (Lower) along the ASR<sub>AT</sub> trajectory. (E) Same data for the ASR<sub>13C</sub> trajectory. (F) Geometrical progression of the reactive bond (C13=C14 for ASR and C11=C12 for Rh) and an adjacent coupled double bond (C15=N for ASR and C9=C10 for Rh) relative to the S<sub>0</sub> equilibrium values.

The slower photoisomerization of ASR<sub>AT</sub> is also consistent with its observed larger fluorescence quantum yield (26). Furthermore, the ASR<sub>AT</sub> model predicts a fluorescence maximum ( $\lambda_{\text{max}}^f$ ) value consistent with the observations. In fact, starting 25 fs after excitation, we compute an average oscillator strength in the 0.8–1.6 range. Taking the average  $\Delta E_{S_1-S_0}$  values over the same 175-fs interval, we predict a fluorescence  $\lambda_{\text{max}}^f$  of 669 nm. A similar analysis can be carried out for ASR<sub>13C</sub>, yielding oscillator strength and fluorescence  $\lambda_{\text{max}}^f$  values of 1.1–1.5 and 665 nm, respectively. Both computed  $\lambda_{\text{max}}^f$  values are comparable with the observed values (i.e., a  $\lambda_{\text{max}}^f$  of 700–710 nm with a shoulder around 650 nm) (26). Also the ASR<sub>AT</sub> trajectory does not decay within the simulation time, consistent with the observed longer fluorescence lifetime with respect to ASR<sub>13C</sub> (26).

It is apparent from inspection of the energy profiles in Fig. 2A–C and from the enlarged views in Fig. 2D and E that both S<sub>1</sub> and S<sub>2</sub> are involved in the isomerizations of ASR<sub>AT</sub> and, partially, of ASR<sub>13C</sub>. Indeed, the corresponding energies become nearly degenerate *ca.* 25 fs after photoexcitation. It is observed that whereas ASR<sub>AT</sub> travels along the degeneracy for the full duration of the trajectory, ASR<sub>13C</sub> abandons the degeneracy region *ca.* 50 fs after entering it and then evolves toward the CI. In contrast, no

degeneracy is found for Rh, which evolves toward the CI directly after photoexcitation. These data support a relationship between the magnitude of the estimated excited state lifetime (defined as the time it takes to reach the CI,  $\tau$ ) and the extent of the S<sub>2</sub>/S<sub>1</sub> mixing. Inclusion of more excited states in the calculations does not change this conclusion (SI Appendix, section 8).

The geometrical progression of PSB11, PSB13, and PSB11 chromophores in the protein are reported in Fig. 2F. The C12–C13–C14–C15 dihedral of ASR<sub>13C</sub>, which describes the isomerization of the C13=C14 bond, changes from 11° to 86°. This motion is coupled with a 13° to –32° change in the C14–C15–N–Cε dihedral describing the torsional deformation of the adjacent C15=N double bond. These results point to a ASR<sub>13C</sub> space-saving S<sub>1</sub> bicycle-pedal isomerization mechanism (36, 37) shared by ASR<sub>AT</sub> in its initial attempt to isomerize (see first 50 fs in Fig. 2F) but distinct from the one reported for Rh (23) and other PSB11-hosting rhodopsins (31) involving the C11=C12 (7) and C9=C10 double bond pair (23, 24, 31). Notice that, in all cases, the bicycle-pedal motion is aborted upon S<sub>1</sub> decay and only one double bond is accomplishing the isomerization (SI Appendix, Fig. S7C) (23, 28). The ASR and Rh isomerization mechanisms are also stereochemically distinct. In fact, whereas in ASR<sub>13C</sub> and ASR<sub>AT</sub> the reactive bond

isomerizes in the counterclockwise direction (with respect to the  $\text{Lys}_{210}$  side chain), in Rh the isomerization occurs in the clockwise direction (with respect to the  $\text{Lys}_{296}$  side chain).

**Origin of the  $S_2/S_1$  Near Degeneracy.** During the first 25 fs after photoexcitation, the rhodopsin chromophore undergoes an inversion in the bond length alternation (BLA) along the backbone (BLA is the difference between the average single bond and the average double bond lengths). For instance, in  $\text{ASR}_{\text{AT}}$ , the  $\text{C13}=\text{C14}$  bond expands from 1.37 to 1.51 Å whereas the  $\text{C14}-\text{C15}$  bond contracts from 1.42 to 1.32 Å. Such a change is accompanied by changes in  $\Delta E_{S_1-S_0}$  and  $\Delta E_{S_2-S_1}$ , which appear as oscillations in the corresponding  $S_0$ ,  $S_1$ , and  $S_2$  energy profiles. We find that, upon BLA relaxation, both  $\text{ASR}_{\text{AT}}$  and  $\text{ASR}_{13\text{C}}$  enter the  $S_2/S_1$  near degeneracy region (see Fig. 2D and E, Upper). Because in the vertical excitation region  $S_1$  has a charge transfer character and  $S_2$  has a diradical character (Fig. 3A), the  $S_1$  electronic structure is perturbed along the trajectory and, for  $\text{ASR}_{\text{AT}}$ , it mixes and even switches from a charge transfer to a diradical charge distribution. This is confirmed by the  $S_0 \rightarrow S_1$  oscillator strength progression, which shows fast recursive variations (Fig. 2D, Lower) of a lower magnitude in  $\text{ASR}_{13\text{C}}$ . The change in electronic character would modify the force field experienced by the  $S_1$  chromophore, resulting in a slower progression toward the CI (because the double bond character of  $\text{C13}=\text{C14}$  is not completely lost in a diradical state and restrains the isomerization).

Notice that, due to potential problems in using the complete active space second-order perturbation theory (CASPT2) method in near degeneracy regions, the  $S_2/S_1$  mixings have been reexamined with a level of theory that does not have such issues (35, 38, 39). We have carried out, for each snapshot of the ASR trajectories, extended multiconfigurational quasi-degenerate second-order perturbation theory (XMCQDPT2) calculations (SI Appendix, section

4) on a model comprising the chromophore surrounded by the point charges of the entire apoprotein. As apparent from inspection of Fig. 2A and B and Fig. 2D and E, the XMCQDPT2 energy displays mostly recurrent avoided crossings rather than CASPT2 crossings.

To explain why a  $S_2/S_1$  near degeneracy region is reached in ASR but not in Rh, we considered the effect of BLA on the different  $S_2$  and  $S_1$  electronic structures (see details in SI Appendix, section 5). Thus, we have investigated the BLA oscillations of specific fragments of the  $\text{ASR}_{\text{AT}}$ ,  $\text{ASR}_{13\text{C}}$  chromophores. In Fig. 3 we compare the BLA values of the  $\text{C5}=\text{C6}-\text{C7}=\text{C8}-\text{C9}=\text{C10}-\text{C11}=\text{C12}-\text{C13}=\text{C14}$  fragment of ASR (Fig. 3B and C) with the corresponding  $\text{C5}=\text{C6}-\text{C7}=\text{C8}-\text{C9}=\text{C10}-\text{C11}=\text{C12}$  fragment of Rh (Fig. 3D). These fragments show marked differences already starting 20 fs after photoexcitation. In particular, the ASR fragments have an average BLA value close to 0.0, indicating similar double and single bond lengths, whereas in Rh the corresponding fragment has negative BLA values consistent with a BLA inversion with respect to its positive  $S_0$  equilibrium value. Notice that  $\text{ASR}_{13\text{C}}$  represents a “transition” between the  $\text{ASR}_{\text{AT}}$  and Rh regimes and its BLA becomes similar to the one of Rh after exiting the  $S_2/S_1$  near degeneracy.

The above observations support the hypothesis that the chromophore type, with its protein-imposed deformation, would control the  $S_1$  relaxations. In fact, the  $\text{ASR}_{\text{AT}}$  relaxation leads to a fragment with four conjugated double bonds ( $\text{C5}=\text{C6}-\text{C7}=\text{C8}-\text{C9}=\text{C10}-\text{C11}=\text{C12}$ ) and an average BLA value consistent with effective delocalization (Fig. 3B). Such a pattern accommodates the diradical electronic structure better than the fragment generated during Rh relaxation (SI Appendix, section 2.2) which, due to the pretwisted  $\beta$ -ionone ring on one side and rapidly twisting  $\text{C11}=\text{C12}$  (Fig. 2F) on the other, offers a shorter fragment with two conjugated double bonds ( $\text{C7}=\text{C8}-\text{C9}=\text{C10}-\text{C11}$ ) with a negative (inverted) average BLA value (32). As a consequence,  $\Delta E_{S_2-S_1}$  will rapidly decrease along the photoisomerization coordinate in  $\text{ASR}_{\text{AT}}$  and  $\text{ASR}_{13\text{C}}$  but not in Rh.

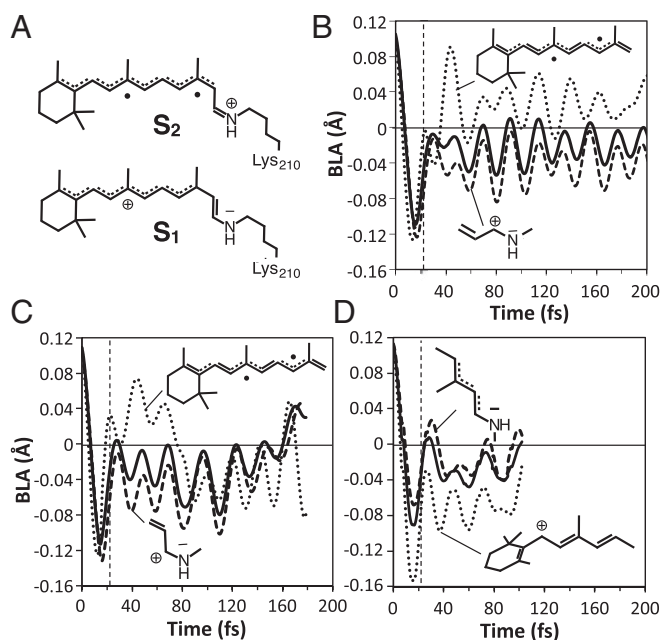


**Fig. 3.** BLA changes in ASR and Rh. (A) Schematic representation of the electronic structure of the  $S_1$  and  $S_2$  states. (B) BLA changes for the  $\text{ASR}_{\text{AT}}$  chromophore along the full conjugated chain (solid line), along the  $\text{C5}=\text{C6}-\text{C7}=\text{C8}-\text{C9}=\text{C10}-\text{C11}=\text{C12}-\text{C13}=\text{C14}$  fragment (dotted line), and along the  $-\text{C13}=\text{C14}-\text{C15}=\text{N}$  fragment (dashed line). (C) Same data for the  $\text{ASR}_{13\text{C}}$  chromophore. (D) The BLA along the full conjugated chain for the Rh chromophore (solid line), along the  $\text{C5}=\text{C6}-\text{C7}=\text{C8}-\text{C9}=\text{C10}-\text{C11}=\text{C12}$  fragment (dotted line), and along the  $-\text{C11}=\text{C12}-\text{C13}=\text{C14}-\text{C15}=\text{N}$  fragment (dashed line).

**Rhodopsin Isomerization in Different Organisms.** As discussed in a previous report (31), photoisomerization quantum yields and thermal isomerization rates are factors determining the level of light sensitivity of rhodopsins. To enhance sensitivity, quantum yields must be maximized whereas thermal rates, which create the “background noise” in the signal, must be minimized. According to a correlation proposed by Weiss and Warshel (6) and Mathies and coworkers (7, 8), for fast impulsive (rather than diffusive) dynamics, the larger the velocity of the  $S_1$  population moving toward the CI the higher the reaction quantum yield. Although the exact nature of such relationship is still under investigation (9, 27), it is apparent that a decrease in the time  $\tau$  required to reach the CI enforces a coherent  $S_1$  dynamics/decay, which, in turn, allows controlling (40) the quantum yield. However, the trend in thermal isomerization rates may be estimated by computing the  $S_0$  isomerization barrier  $E_a^{\text{T}}$ . Thus, the  $\tau$  and  $E_a^{\text{T}}$  values of ASR together with those previously reported for Rh, squid rhodopsin (sqRh), and human melanopsin (hMeOp) (31) can be used to model trends of light sensitivity. Indeed, the  $\text{ASR}_{13\text{C}}$ , Rh, sqRh, and hMeOp  $\tau$  values in Fig. 4A suggest a somehow exponential increase of  $\tau$  when  $\lambda_{\text{max}}^a$  increases. However, the long  $S_1$  lifetime observed for  $\text{ASR}_{\text{AT}}$  does not fit in. Thus, whereas an increase of  $\tau$  may be associated with a decrease in slope of the  $S_1$  potential energy surface accelerating progression toward the CI (Fig. 4B), in  $\text{ASR}_{\text{AT}}$  and other PSBAT-hosting rhodopsins the occurrence of the  $S_2/S_1$  degeneracy changes the dynamics (Fig. 4C), which becomes slower and complex with an increased fluorescence lifetime. The  $S_1$  relaxation would thus be more diffusive with the chromophore exploring the rugged potential energy surface shaped by several  $S_2/S_1$  avoided crossings (Fig. 3D, Lower) and, as a consequence, the velocity–quantum yield relationship loses its



- Ernst OP, et al. (2014) Microbial and animal rhodopsins: Structures, functions, and molecular mechanisms. *Chem Rev* 114(1):126–163.
- Devine EL, Oprrian DD, Theobald DL (2013) Relocating the active-site lysine in rhodopsin and implications for evolution of retinylidene proteins. *Proc Natl Acad Sci USA* 110(33):13351–13355.
- Mackin KA, Roy RA, Theobald DL (2014) An empirical test of convergent evolution in rhodopsins. *Mol Biol Evol* 31(1):85–95.
- Sharma AK, Spudich JL, Doolittle WF (2006) Microbial rhodopsins: Functional versatility and genetic mobility. *Trends Microbiol* 14(11):463–469.
- Shichida Y, Matsuyama T (2009) Evolution of opsins and phototransduction. *Philos Trans R Soc Lond B Biol Sci* 364(1531):2881–2895.
- Weiss RM, Warshel A (1979) A new view of the dynamics of singlet cis-trans photoisomerization. *J Am Chem Soc* 101(20):6131–6133.
- Schoenlein RW, Peteanu LA, Mathies RA, Shank CV (1991) The first step in vision: Femtosecond isomerization of rhodopsin. *Science* 254(5030):412–415.
- Kim JE, Tauber MJ, Mathies RA (2003) Analysis of the mode-specific excited-state energy distribution and wavelength-dependent photoreaction quantum yield in rhodopsin. *Biophys J* 84(4):2492–2501.
- Schapiro I, et al. (2011) The ultrafast photoisomerizations of rhodopsin and bathorhodopsin are modulated by bond length alternation and HOOP driven electronic effects. *J Am Chem Soc* 133(10):3354–3364.
- Weingart O, et al. (2011) Product formation in rhodopsin by fast hydrogen motions. *Phys Chem Chem Phys* 13(9):3645–3648.
- Sakmar TP, Franke RR, Khorana HG (1989) Glutamic acid-113 serves as the retinylidene Schiff base counterion in bovine rhodopsin. *Proc Natl Acad Sci USA* 86(21):8309–8313.
- Fujimoto K, Hasegawa J-Y, Hayashi S, Kato S, Nakatsuji H (2005) Mechanism of color tuning in retinal protein: SAC-CI and QM/MM study. *Chem Phys Lett* 414:239–242.
- Coto PB, Strambi A, Ferré N, Olivucci M (2006) The color of rhodopsins at the ab initio multiconfigurational perturbation theory resolution. *Proc Natl Acad Sci USA* 103(46):17154–17159.
- Hoffmann M, et al. (2006) Color tuning in rhodopsins: The mechanism for the spectral shift between bacteriorhodopsin and sensory rhodopsin II. *J Am Chem Soc* 128(33):10808–10818.
- Ryazantsev MN, Altun A, Morokuma K (2012) Color tuning in rhodopsins: The origin of the spectral shift between the chloride-bound and anion-free forms of halorhodopsin. *J Am Chem Soc* 134(12):5520–5523.
- Sekharan S, Morokuma K (2011) Why 11-cis-retinal? Why not 7-cis-, 9-cis-, or 13-cis-retinal in the eye? *J Am Chem Soc* 133(47):19052–19055.
- Sineshchekov OA, Trivedi VD, Sasaki J, Spudich JL (2005) Photochromicity of Anabaena sensory rhodopsin, an atypical microbial receptor with a cis-retinal light-adapted form. *J Biol Chem* 280(15):14663–14668.
- Hofmann KP, et al. (2009) A G protein-coupled receptor at work: The rhodopsin model. *Trends Biochem Sci* 34(11):540–552.
- Kukura P, McCamant DW, Yoon S, Wandschneider DB, Mathies RA (2005) Structural observation of the primary isomerization in vision with femtosecond-stimulated Raman. *Science* 310(5750):1006–1009.
- Kandori H, Shichida Y, Yoshizawa T (2001) Photoisomerization in rhodopsin. *Biochemistry (Mosc)* 66(11):1197–1209.
- Wang Q, Schoenlein RW, Peteanu LA, Mathies RA, Shank CV (1994) Vibrationally coherent photochemistry in the femtosecond primary event of vision. *Science* 266(5184):422–424.
- Andruniów T, Ferré N, Olivucci M (2004) Structure, initial excited-state relaxation, and energy storage of rhodopsin resolved at the multiconfigurational perturbation theory level. *Proc Natl Acad Sci USA* 101(52):17908–17913.
- Frutos LM, Andruniów T, Santoro F, Ferré N, Olivucci M (2007) Tracking the excited-state time evolution of the visual pigment with multiconfigurational quantum chemistry. *Proc Natl Acad Sci USA* 104(19):7764–7769.
- Polli D, et al. (2010) Conical intersection dynamics of the primary photoisomerization event in vision. *Nature* 467(7314):440–443.
- Wand A, et al. (2011) Asymmetric toggling of a natural photoswitch: Ultrafast spectroscopy of Anabaena sensory rhodopsin. *J Am Chem Soc* 133(51):20922–20932.
- Cheminal A, et al. (2013) Steady state emission of the fluorescent intermediate of Anabaena Sensory Rhodopsin as a function of light adaptation conditions. *Chem Phys Lett* 587:75–80.
- Cheminal A, et al. (2015) 100 fs photo-isomerization with vibrational coherences but low quantum yield in Anabaena Sensory Rhodopsin. *Phys Chem Chem Phys* 17(38):25429–25439.
- Strambi A, Durbeej B, Ferré N, Olivucci M (2010) Anabaena sensory rhodopsin is a light-driven unidirectional rotor. *Proc Natl Acad Sci USA* 107(50):21322–21326.
- Schapiro I, Ruhman S (2014) Ultrafast photochemistry of anabaena sensory rhodopsin: Experiment and theory. *Biochim Biophys Acta* 1837(5):589–597.
- Warshel A, Levitt M (1976) Theoretical studies of enzymic reactions: dielectric, electrostatic and steric stabilization of the carbonium ion in the reaction of lysozyme. *J Mol Biol* 103(2):227–249.
- Rinaldi S, Melaccio F, Gozem S, Fanelli F, Olivucci M (2014) Comparison of the isomerization mechanisms of human melanopsin and invertebrate and vertebrate rhodopsins. *Proc Natl Acad Sci USA* 111(5):1714–1719.
- Cembran A, Bernardi F, Olivucci M, Garavelli M (2004) Counterion controlled photoisomerization of retinal chromophore models: A computational investigation. *J Am Chem Soc* 126(49):16018–16037.
- Cembran A, et al. (2005) Structure, spectroscopy, and spectral tuning of the gas-phase retinal chromophore: The beta-ionone “handle” and alkyl group effect. *J Phys Chem A* 109(29):6597–6605.
- Gozem S, et al. (2014) On the shape of multireference, EOM-CC, and DFT potential energy surfaces at a conical intersection. *J Chem Theory Comput* 10(8):3074–3084.
- Granovsky AA (2011) Extended multi-configuration quasi-degenerate perturbation theory: The new approach to multi-state multi-reference perturbation theory. *J Chem Phys* 134(21):214113.
- Warshel A (1976) Bicycle-pedal model for the first step in the vision process. *Nature* 260(5553):679–683.
- Altoè P, Cembran A, Olivucci M, Garavelli M (2010) Aborted double bicycle-pedal isomerization with hydrogen bond breaking is the primary event of bacteriorhodopsin proton pumping. *Proc Natl Acad Sci USA* 107(47):20172–20177.
- Gozem S, et al. (2012) Dynamic electron correlation effects on the ground state potential energy surface of a retinal chromophore model. *J Chem Theory Comput* 8:4069–4080.
- Malrieu J-P, Heully J-L, Zaitsevskii A (1995) Multiconfigurational second-order perturbative methods: Overview and comparison of basic properties. *Theor Chim Acta* 90:167–187.
- Brumer P, Shapiro M (1997) Quantum interference in the control of molecular processes. *Phil. Trans. R. Soc. A* 355:2409–2412.
- Yabushita A, Kobayashi T, Tsuda M (2012) Time-resolved spectroscopy of ultrafast photoisomerization of octopus rhodopsin under photoexcitation. *J Phys Chem B* 116(6):1920–1926.
- Gai F, Hasson KC, McDonald JC, Anfinrud PA (1998) Chemical dynamics in proteins: The photoisomerization of retinal in bacteriorhodopsin. *Science* 279(5358):1886–1891.
- Garavelli M, Celani P, Bernardi F, Robb MA, Olivucci M (1997) Force fields for “ultrafast” photochemistry: The S2 (1Bu) → S1 (2Ag) → S0 (1Ag) reaction path for all-trans-Hexa-1,3,5-triene. *J Am Chem Soc* 119:11487–11494.
- Cembran A, González-Luque R, Serrano-Andrés L, Merchán M, Garavelli M (2007) About the intrinsic photochemical properties of the 11-cis retinal chromophore: Computational clues for a trap state and a lever effect in Rhodopsin catalysis. *Theor Chem Acc* 118(1):173–183.
- Dokukina I, Weingart O (2015) Spectral properties and isomerisation path of retinal in C1C2 channelrhodopsin. *Phys Chem Chem Phys* 17(38):25142–25150.
- Briand J, Léonard J, Haacke S (2010) Ultrafast photo-induced reaction dynamics in bacteriorhodopsin and its Trp mutants. *J Opt* 12(8):084004.
- Bassolino G, et al. (2014) Synthetic control of retinal photochemistry and photophysics in solution. *J Am Chem Soc* 136(6):2650–2658.
- Cembran A, Bernardi F, Olivucci M, Garavelli M (2005) The retinal chromophore/chloride ion pair: Structure of the photoisomerization path and interplay of charge transfer and covalent states. *Proc Natl Acad Sci USA* 102(18):6255–6260.
- Zgrablić G, Voitchovsky K, Kindermann M, Haacke S, Chergui M (2005) Ultrafast excited state dynamics of the protonated Schiff base of all-trans retinal in solvents. *Biophys J* 88(4):2779–2788.
- Munoz-Losa A, Martín ME, Fernández Galván I, Sánchez ML, Aguilar M (2011) Solvent effects on the radiative and non-radiative decay of a model of the rhodopsin chromophore. *J Chem Theory Comput* 7:4050–4059.
- Muñoz-Losa A, Ignacio I, Aguilar MA, Martín ME (2013) Simultaneous solvent and counterion effects on the absorption properties of a model of the rhodopsin chromophore. *J Chem Theory Comput* 9(3):1548–1556.
- Barlow HB (1957) Purkinje shift and retinal noise. *Nature* 179(4553):255–256.
- Ala-Laurila P, Donner K, Koskelainen A (2004) Thermal activation and photoactivation of visual pigments. *Biophys J* 86(6):3653–3662.
- Gozem S, Schapiro I, Ferré N, Olivucci M (2012) The molecular mechanism of thermal noise in rod photoreceptors. *Science* 337(6099):1225–1228.
- Sudo Y, et al. (2011) A microbial rhodopsin with a unique retinal composition shows both sensory rhodopsin II and bacteriorhodopsin-like properties. *J Biol Chem* 286(8):5967–5976.
- Vogel L, et al. (2004) Anabaena sensory rhodopsin: A photochromic color sensor at 2.0 Å. *Science* 306(5700):1390–1393.
- Aquilante F, et al. (2010) MOLCAS 7: the next generation. *J Comp Chem* 31(1):224–247.
- Ponder JW, Richards FM (1987) An efficient newton-like method for molecular mechanics energy minimization of large molecules. *J Comp Chem* 8(7):1016–1024.
- Roos BO (1987) The complete active space self-consistent method and its applications in electronic structure calculations. *Ab Initio Methods in Quantum Chemistry*, Advances in Chemical Physics, ed Lawley KP (Wiley, New York), Pt 2, Vol 69, pp 399–445.
- Andersson K, Malmqvist PA, Roos BO, Sadlej AJ, Wolinski K (1990) Second-order perturbation theory with a CAS-SCF reference function. *J Phys Chem* 94:5483–5488.
- Granovsky AA (2014) Firefly. Available at classic.chem.msu.edu/gran/firefly/index.html. Version 8.0.0.